Kent Academic Repository

Induced chemistry by scattering of electrons from magnesium oxide

Minaxi Vinodkumar[*]

VP & RPTP Science College, Vallabh Vidyanagar-388120, India

Hardik Desai[†] and P. C. Vinodkumar[‡]

Department of Physics, Sardar Patel University, Vallabh Vidyanagar-388120, India

Nigel Mason[§]

Department of Physical Sciences, Open University, Milton Keynes MK76AA, United Kingdom

A detailed theoretical study is carried out for electron interactions with magnesium oxide (MgO) with incident energies ranging from 0.01 to 5000 eV. This wide range of energy has allowed us to investigate a variety of processes and report data on resonances through eigenphase study, vertical electronic excitation energies, differential, momentum transfer, and total cross sections (TCS), as well as scattering rate coefficients. MgO has a large number of low-lying π excited states and the present study finds overall a good agreement with earlier reported data. In order to compute total cross sections, we have employed the *ab initio R*-matrix method (0.01 to ~20 eV) and the spherical complex optical potential method (~20 to 5000 eV). The *R*-matrix calculations are performed using a close-coupling method with the aid of 34 target states, 1436 configuration state functions, and 213 channels employing a static exchange plus polarization model. The present study reports evidence for electron scattering resonances through analysis of eigenphase diagrams at low energies below the ionization threshold. In the absence of any theoretical or experimental data for resonances, we have done double differentiation of TCS to confirm the resonances reported here. The present study is a maiden effort to report excitation cross sections, differential cross sections, momentum transfer cross sections, and scattering rate coefficients at low energies below the ionization threshold of the target. Additionally, in the absence of any experimental data and sparse theoretical data for a total elastic cross section, the present comprehensive study will provide a reference data set over such an extensive impact energy range.

I. INTRODUCTION

With the advent of highly sophisticated instruments for experiments and high-performing computers for computation, accurate electron collision data is a great success. However, such methods are quite tedious and require both considerable manpower and computational resources, producing only a limited number of electron scattering cross sections for limited targets out of the ocean of molecular systems that need to be studied due to their importance in many diverse areas of science and technology. This has prompted the authors to look for faster methods to derive electron impact collision data on the time scales required by the applied industry.

In the present paper, we focus on the calculation of electron collisions with magnesium oxide over a wide range of impact energies from 0.01 to 5000 eV. MgO is a simple diatomic molecule distinguished from other alkaline-earth metal oxides because it has several closely low-lying π excited states [1], which has led to extensive spectroscopic studies of MgO [1–12]. There is tremendous work on electronic excitation energies of MgO both theoretically [1–5] and experimentally [6–11]. Besides spectroscopy, thermochemical investigation has also increased due to its use as a catalyst

in the hydrocarbon reaction [13]. Further, MgO is widely used as the protective layer in plasma display panels (PDPs) because it has good characteristics of secondary electron emission [14]. Additionally, MgO has been identified in the interstellar medium, stimulating interest among the astrochemistry community [15,16]. A literature survey emphasizes the fact that there has been a large amount of work on the ground state and electronic excitation states of MgO, but the collision data is extremely sparse. There are no experimental studies of electron impact collision partly because it is difficult to obtain pure samples of MgO in the gaseous phase [17], and only one previous theoretical calculation by Dapor and Miotello [18] who reported a decade ago for total elastic and total transport elastic cross sections for *e*-MgO scattering from 50 eV to 10 keV. This large void in the collision data prompted us to do the present study.

In this paper, we have performed scattering calculations separately over two energy regimes (0.01 to 20 eV and ionization threshold to 5000 eV). In the low-energy region (below the vertical ionization potential), we make use of the UK molecular *R*-matrix code [19,20]. In the intermediate- and high-energy region (above the vertical ionization potential), we employ the spherical complex optical potential (SCOP) formalism [21,22]. Our low-energy study below 10 eV is significant owing to the formation of short-lived anions (resonances) and thus the possibility of their decay to produce neutral and anionic fragments. Such processes are very important in understanding the local chemistry induced by electron target interaction. The present study is a maiden effort

[*]minaxivinod@yahoo.co.in

[†]hardikdesai.phy@gmail.com

[‡]p.c.vinodkumar@gmail.com

[§]n.j.mason@open.ac.uk

to report resonances through eigenphase study, excitation cross sections, differential cross sections, momentum transfer cross sections, and total cross sections at low energies below the ionization threshold of the target.

II. THEORETICAL METHODOLOGY

Before providing details on the two theoretical methodologies (R matrix and SCOP) adopted for the present study, we discuss the target model employed in the low-energy calculation.

Target model used for low-energy calculations

For precise target properties as well as for the scattering data, it is imperative to have an appropriate target model. Magnesium oxide is a linear diatomic molecule with an ionic bond between magnesium and oxygen with an equilibrium bond distance of 1.749 Å [23]. We have employed a 6-311G* basis set for the target wave-function representation. MgO has C∞ symmetry, but we have used C_{2v} point-group symmetry to reduce the computational complexity in the wave-function representation. The major key parameters involved in a proper choice of the configurations are complete active space (CAS) and the valance configuration interaction (CI) representation of the target system [24]. It is achieved by carefully characterizing the low-lying electronic states of the target and by generating a suitable set of molecular orbitals. The molecular orbitals are generated by performing a self-consistent field (SCF) calculation of the ground state of the molecule (X $1A_1$). Since the SCF procedure is not adequate to provide a good representation of the target states, we improve the energies of these states by employing the variational method of configuration interaction (CI) in which we take a linear combination of the configuration state functions (CSFs) of a particular overall symmetry. This not only lowers the energies of these states, but also the correlation introduced provides a better representation of the charge cloud and the energies.

For the 34 target states included here, we employ a CI wave function to represent them. The Hartree-Fock electronic configuration for the ground state of MgO at its equilibrium geometry in the C_{2v} point-group symmetry is $1a_1^2$, $2a_1^2$, $3a_1^2$, $1b_1^2$, $1b_2^2$, $4a_1^2$, $5a_1^2$, $2b_2^2$, $2b_1^2$, and $6a_1^2$. Out of 20 electrons, we froze 12 electrons in six molecular orbitals $1a_1$, $2a_1$, $3a_1$, $4a_1$, $1b_1$, and $1b_2$. The rest of the eight electrons are allowed to move

freely in the active space of nine target occupied and virtual molecular orbitals $5a_1$, $6a_1$, $7a_1$, $8a_1$, $9a_1$, $2b_1$, $3b_1$, $2b_2$, and $3b_2$. Seven virtual molecular orbitals (two of A_1 symmetry, two of B_1 symmetry, two of B_2 symmetry, and one of A_2 symmetry) are used to augment the continuum orbitals. A total of 34 target states were included in the close-coupling calculations involving 1436 configuration state functions (CSFs) for the ground state, and the number of channels included in the calculation is 213.

The R-matrix inner-region modules GAUSPROP and DENPROP generate target properties using Hartree-Fock calculations and construct the transition density matrix from the target eigenvectors obtained from configuration interaction (CI) calculations [25]. The multipole transition moments obtained are then used to solve the outer-region coupled equations and the dipole polarizability α_0. These are computed using second-order perturbation theory and the property integrals are evaluated by GAUSPROP.

The self-consistent field (SCF) calculation yielded the ground-state energy of MgO as -274.4167 hartree, which is in very good agreement with theoretical values of -274.3901, -274.3866, and -274.4655 hartree reported by Piyykko *et al.* [26], McLean and Yahimine [27], and Bauschlicher *et al.* [2], respectively. The first electronic excitation energy of MgO is found to be 0.3428 eV, which is in very good agreement with the experimental value of 0.3112 eV reported by Kim *et al.* [8] and 0.3252 eV reported by Ikeda *et al.* [11]. Such a low electronic excitation energy is expected since it has very closely low-lying π excited states [2,3]. The present computed rotational constant of MgO is 0.5743 cm^{-1}, which is in good agreement with the experimental value of 0.5748 cm^{-1} reported by Murtz *et al.* [28]. The calculated dipole moment of 6.2 Debye is also in excellent agreement with the dipole moment of 6.2 ± 0.6 Debye reported in the *CRC Handbook of Chemistry and Physics* [23]. Present calculations for the ionization potential (IP) resulted in 8.49 eV, which is in good agreement with 8.76 eV reported in the CRC Handbook [23] and in excellent agreement with 8.76 ± 0.22 eV reported in the NIST Computational Chemistry Comparison and Benchmark Database (CCCBDB) [29]. The target properties along with available comparisons are listed in Table I. Thus, a very good reproduction of all of the target properties assures a very good target model, which in turn guarantees reliable collision cross-section data. A large number (34) of electronic excitation thresholds for magnesium oxide obtained here are listed in

TABLE I. Target properties of magnesium oxide.

Target property (unit)		Present	Other	
			Theory	Expt.
Ground-state energy (hartree)		-274.4167	-274.3901 [26] -274.3866 [27] -274.4655 [2]	
First excitation energy (eV)		0.3428		0.3112 [8] 0.3252 [11]
Rotational constant (cm^{-1})	B	0.5743		0.5748 [28]
Dipole moment (Debye)		6.2		6.2 ± 0.6 [23]
Ionization potential (eV)		8.49		8.76 [23] 8.76 ± 0.22 [29]

TABLE II. Vertical excitation energy of **MgO** molecule for all excited states below 9 eV. The target states are designated in C_{2v} ($C_{\infty v}$) symmetry.

State	Present (eV)	Other (eV) Theory	Other (eV) Expt.
1 $^1A_1$ (X $^1\Sigma^+$)	0.0000		0.0000
1 $^3B_1$, $^3B_2$ (1 $^3\Pi$)	0.3428	0.2688 [3], 0.2914 [1], 0.3230 [2], 0.2381 [5]	0.3112 [8], 0.3252 [11]
1 $^1B_1$, $^1B_2$ (1 $^1\Pi$)	0.4109	0.4083 [3], 0.4398 [1,2], 0.3305 [5]	0.4203 [8], 0.4399 [6,10–12], 0.4418 [7]
1 $^1A_1$ (1 $^3\Sigma^+$)	0.7564	1.0212 [3], 1.0823 [2], 1.0432 [5]	
2 $^1A_1$ (2 $^1\Sigma^+$)	2.7346	2.5684 [3], 2.6089 [2], 2.4672 [1], 2.5060 [5]	2.4797 [8], 2.4672 [6,7]
2 $^3A_1$ (2 $^3\Sigma^+$)	4.0679	3.4141 [3], 3.4630 [1], 3.4981 [5]	
3 $^3A_1$, $^3A_2$ (3 $^3\Delta$)	4.1876	3.5470 [3], 3.4679 [1], 3.6587 [5], 3.6698 [5]	3.2650 [7]
3 $^1A_1$, $^1A_2$ (3 $^1\Delta$)	4.2312	3.6585 [3], 3.6833 [1], 3.7231 [5]	3.7116 [10], 3.8534 [6], 3.2933 [7]
2 $^3A_2$ (2 $^3\Sigma^-$)	4.2720	3.7111 [1], 3.9117 [5]	
2 $^1A_2$ (2 $^1\Sigma^-$)	4.2856	4.5333 [1]	
2 $^3B_2$, $^3B_1$ (2 $^3\Pi$)	4.7944	4.7630 [1]	3.7011 [6]
2 $^1B_1$, $^1B_2$ (2 $^1\Pi$)	4.8760	4.8827 [1], 4.8297 [5]	
3 $^3B_2$, $^3B_1$ (3 $^3\Pi$)	5.6434	5.2963 [1]	
3 $^1B_1$, $^1B_2$ (3 $^1\Pi$)	5.7985	5.4346 [1]	
4 $^3A_1$ (4 $^3\Sigma^+$)	6.2746	6.6519 [1]	
4 $^1A_1$ (4 $^1\Sigma^+$)	6.3726	6.8519 [1]	
4 $^3B_2$, $^3B_1$ (4 $^3\Pi$)	6.7835		
4 $^1B_2$, $^1B_1$ (4 $^1\Pi$)	6.8542		
5 $^1A_1$ (5 $^1\Sigma^+$)	6.8705		
5 $^3A_1$ (5 $^3\Sigma^+$)	7.3467		
6 $^1A_1$ (6 $^1\Sigma^+$)	7.7848		
5 $^3B_2$, $^3B_1$ (5 $^3\Pi$)	8.8133		
3 $^3A_2$ (3 $^3\Sigma^-$)	8.9983		

Table II. It is quite evident from Table II that our reported vertical excitation energies are in very good agreement overall with the earlier predicted experimental [6,7,11] as well as theoretical results [1,2,5]. Here, vertical excited-state energies beyond 4 $^1A_1$ are predicted.

Low-energy formalism (0.01–15 eV)

Currently, low-energy electron collisions are modeled using the Kohn variational method [30,31], the Schwinger variational method [32–34], and the *R*-matrix method, of which *R* matrix [19,20,35,36] is the most widely used method. The underlying idea behind the *R*-matrix method relies on the division of configuration space into two spatial regions: an inner region and outer region. The inner region radius is chosen large enough so that in the external region, only known long-range forces are effective and antisymmetrization effects can be neglected, which makes the outer-region calculations very simple. The inner region involves short-range potentials arising due to electron-electron correlation and exchange, which makes the calculation very complex. In the inner region, the full electron-molecule problem is solved using quantum chemistry codes. The inner region is usually chosen to have a radius of around 10 a.u. and the outer region is extended to about 100 a.u. The choice of this value depends on the stability of results obtained in the inner-region and outer-region calculations.

We describe the scattering within the fixed-nuclei (FN) approximation that neglects any dynamics involving the nuclear motion (rotational as well as vibrational), whereas the bound electrons are taken to be in the ground electronic state of the target at its optimized nuclear geometry. This is an effect of the extent of electronic charge density distribution around the center of mass of the target. The center of this sphere is chosen at the center of mass of the target; thus, *N*-target electrons plus one incident electron are contained in the inner region, which makes the problem numerically complex but physically very precise. Consequently, the accuracy of the scattering calculation depends critically on how the inner-region physics is defined. The solution of the inner-region problem involves rigorous computation using quantum chemistry codes and this is the major time constraint of the calculation. Interestingly, the inner-region problem is solved independent of the energy of the scattering electron and hence is done only once.

In the outer region when the scattering electron is at a large distance from the center of mass of the target, the probability of swapping its identity with any one of the target electrons is negligible, resulting in negligible contributions from exchange and correlation effects. The single-center close-coupling approximation with direct potential leads to a set of coupled differential equations, allowing for quick, simple, and fast solutions in the outer region. The outer-region calculations are repeated for each set of energies. In the present calculations, the inner *R*-matrix radius is taken as $13a_o$ owing to the larger size of the target. In the outer region, the *R* matrix on the boundary is propagated to a sufficiently large distance such that the interaction potential between target electrons and the scattering electron is assumed to be zero. In the present case, this distance is $100a_o$. Asymptotic expansion techniques are used to solve the outer-region functions [37].

In the inner region, the target electrons are placed in some combination of target molecular orbitals, which are represented by Gaussian-type orbitals and are multiplied by spin functions to generate configuration state functions (CSFs). The target molecular orbitals are also supplemented by a set of continuum orbitals which have longer range and extend beyond the inner-region R-matrix boundary. In the inner region, the wave function is constructed using the close-coupling approximation for all $N + 1$ electrons [38]. The total wave function for the system may then be given as

$$\Psi_k^{N+1}(x_1 \ldots x_{N+1}) = A \sum_{ij} a_{ijk} \Phi_i^N(x_1 \ldots x_N) u_{ij}(x_{N+1})$$
$$+ \sum_i b_{ik} \chi_i^{N+1}(x_1 \ldots x_{N+1}), \quad (1)$$

where A is the antisymmetrization operator that takes care of exchange effects among the $N + 1$ electrons, x_N (r_n, σ_n) is the spatial and spin coordinate of the nth electron, and $_j$ is a continuum molecular orbital that is spin coupled with the scattering electron. a_{ijk} and b_{ik} are variational coefficients determined by the diagonalization of the $N + 1$ Hamiltonian matrix.

The accuracy of the calculation depends solely on the precise construction of the wave function given in Eq. (1). The first summation runs over the 34 target states used in the close-coupled expansion and a static-exchange calculation has a single Hartree-Fock target state in the first sum. Here one electron is placed in the continuum orbital of the target and the rest of the electrons move in available target molecular orbitals, thus generating a target + continuum configuration. In the second term, χ_m are multicenter quadratically integrable functions, known as L^2 functions, constructed from target occupied and virtual molecular orbitals, and are used to represent correlation and polarization effects. This sum runs over a minimal number of configurations, usually three or fewer, which is required to relax orthogonality constraints between the target molecular orbitals and the functions used to represent the configuration. The continuum orbitals are centered on the center of mass of the molecule.

The complete molecular orbital representation in terms of occupied and virtual target molecular orbitals is constructed using the Hartree-Fock self-consistent field method with Gaussian-type orbitals (GTOs) and the continuum orbitals of Faure *et al.* [39], and include up to g ($l = 4$) orbitals. The benefit of employing a partial wave expansion for the low-energy electron molecule interaction is its rapid convergence. In the case of dipole-forbidden excitations ($\Delta J \neq 1$), where J represents a rotational quantum number, the convergence of the partial waves is rapid, but in the case of dipole-allowed excitations ($\Delta J = 1$) the partial wave expansion converges slowly due to the long-range nature of the dipole interaction. In order to account for the higher partial waves not included in the fixed-nuclei T matrices, the effect of partial waves higher than $l = 4$ was included using a Born correction, which requires expressions for the partial waves as well as full Born cross sections. These expressions are taken from the work of Chu and Dalgarno [40]. We are constrained to employ partial waves for the continuum orbital up to $l = 4$ only, as the representation in Gaussian-type orbitals for the Bessel functions higher than

$l = 4$ is not available. For low partial waves ($l \leqslant 4$), T matrices computed from the R-matrix calculations are employed to compute the cross sections. The low partial wave contribution arising from the Born contribution is subtracted in order that the final cross-section set only contains those partial waves due to the R-matrix calculation. We have performed the calculations with and without dipole Born correction.

The R matrix provides the link between the inner region and the outer region. The R matrix is propagated to an asymptotic region where the radial wave functions describing the scattering electron can be matched to analytical expressions. For this purpose, the inner region is propagated to the outer-region potential until its solution matches the asymptotic functions given by the Gailitis expansion [41]. Coupled single-center equations describing the scattering in the outer region are integrated to identify the K-matrix elements. The K matrix is a symmetric matrix whose dimensions are the number of open channels. All of the observables deduced from it can be used to obtain T matrices using the definition

$$T = \frac{2iK}{1 - iK}. \quad (2)$$

The T matrices are, in turn, used to obtain various total cross sections. The K matrix is diagonalized to obtain the eigenphase sum. The eigenphase sum is further used to obtain the position and width of any scattering resonances by fitting them to a Breit-Wigner profile [42]. The detailed procedure is described in our earlier publications [21,22,43,44].

Differential cross sections (DCS) are very important as they provide a large amount of information about the interaction process which is generally averaged out in the total cross section. Indeed, the evaluation of DCS is a rigorous test for any scattering theory. The DCS for a polyatomic molecule is represented by

$$\frac{d\sigma}{d\Omega} = \sum_L A_L P_L(\cos\theta), \quad (3)$$

where P_L is the Legendre polynomial. Details on A_L have been discussed by Gianturco and Jain [45]. For a polar molecule, this expansion over L converges slowly due to the long-range nature of the dipole potential. To overcome this problem, we use the closure formula given by

$$\frac{d\sigma}{d\Omega} = \frac{d\sigma^B}{d\Omega} + \sum_L \left(A_L - A_L^B\right) P_L \cos\theta, \quad (4)$$

where B denotes the fact that the relevant term is calculated under the conditions of the Born approximation with an electron point dipole interaction. It is clear from the above expression that convergence of the series is faster compared to calculations with no Born corrections since the contribution from higher partial waves is dominated by the dipole interaction. Differential and momentum transfer cross sections (MTCS) are calculated using the POLYDCS program with the MTCS obtained by integrating the differential cross sections (DCS) with a weighting factor $(1 - \cos\theta)$ [46].

III. HIGH-ENERGY FORMALISM

Even with the aid of the latest computing facilities, the *R*-matrix code has limitations for scattering calculations beyond 20 eV, and hence intermediate- to high-energy electron scattering is modeled here using the SCOP formalism [43,44,47,48]. We employ a partial wave analysis to solve the Schrödinger equation with various model potentials as its input. The interaction of the incoming electron with the target molecule can be represented by a complex optical potential (V_{opt}), which can be partitioned into real (V_R) and imaginary (V_I) parts as

$$V_{opt}(E_i, r) = V_R(E_i, r) + i V_I(E_i, r), \quad (5)$$

such that

$$V_R(E_i, r) = V_{st}(E_i, r) + V_{ex}(E_i, r) + V_p(E_i, r), \quad (6)$$

where the real part V_R is composed of the static potential (V_{st}), exchange potential (V_{ex}), and polarization potential (V_p). The static potential (V_{st}) arises from the Coulombic interaction between the static charge distribution of the target and the projectile. It is calculated at the Hartree-Fock level. The exchange potential (V_{ex}) term accounts for the electron exchange interaction between the incoming projectile and one of the target electrons. The polarization potential (V_p) represents the short-range correlation and long-range polarization effect arising from the temporary redistribution of the target charge cloud. Note that the spherical complex optical potential as such does not require any fitting parameters. The most important basic input for evaluating all of these potentials is the charge density of the target. The complexity of electron molecule scattering is reduced by adopting a single-center approach so as to make the spherical approximation applicable [49,50].

In the case of MgO, the single-center charge density is obtained by expanding the charge density of the Mg atom and O atom at the center of mass of the system. The spherically averaged molecular charge density is determined from the constituent atomic charge densities using the Hartree-Fock wave functions of Bunge *et al.* [51]. The molecular charge density so obtained is then renormalized to incorporate the covalent bonding [49,51]. In the SCOP method, the spherical

part of the complex optical potential is treated exactly in a partial wave analysis to yield various cross sections [49].

The atomic charge densities and static potentials (V_{st}) are formulated from the parameterized Hartree-Fock wave functions given by Bunge *et al.* [51]. The parameter-free Hara's "free-electron gas exchange model" is used to generate the exchange potential (V_{ex}) [52]. The polarization potential (V_p) is constructed from the parameter-free model of correlation-polarization potential given by Zhang *et al.* [53]. Here, various multipole nonadiabatic corrections are incorporated into the intermediate region, which approaches the correct asymptotic form at large r smoothly.

The imaginary part in V_{opt} is called the absorption potential, and V_{abs} or V_I accounts for the total loss of flux scattered into the allowed electronic excitation or ionization channels. The V_{abs} is not a long-range effect and its penetration towards the origin increases with increasing energy. This implies that at high energies, the absorption potential accounts for the inner-shell excitations or ionization processes that may be closed at low energies.

The well-known quasifree model form of Staszewska *et al.* [54,55], employed for the absorption part, is given by

$$V_{abs}(r, E_i) = -\rho(r)\sqrt{\frac{T_{loc}}{2}}\left(\frac{8\pi}{10 k_F^3 E_i}\right)$$
$$\times \theta\left(p^2 - k_F^2 - 2\Delta\right)(A_1 + A_2 + A_3), \quad (7)$$

where the local kinetic energy of the incident electron is

$$T_{loc} = E_i - (V_{st} + V_{ex} + V_p), \quad (8)$$

where $p^2 = 2E_i$, $k_F = [3\pi^2\rho(r)]^{\frac{1}{3}}$ is the Fermi wave vector, and A_1, A_2, and A_3 [44] are dynamic functions that depend differently on $\theta(x)$, I, Δ, and E_i. I is the ionization threshold of the target, $\theta(x)$ is the Heaviside unit step function and is an energy parameter below which $V_{abs} = 0$. Hence, Δ is the principal factor which decides the value of the total inelastic cross section since below this value, ionization or excitation is not permissible. This is one of the main characteristics of the Staszewska model [54,55]. We have attempted this by considering Δ as a slowly varying function of E_i around I. Such an approximation is meaningful since Δ fixed at I would not allow

TABLE III. Total cross sections (TCSs) for *e*-MgO scattering.

Energy (eV)	*R* matrix TCS (Å^2)	Energy (eV)	*R* matrix TCS (Å^2)	Energy (eV)	*R* matrix TCS (Å^2)	Energy (eV)	SCOP TCS (Å^2)	Energy (eV)	SCOP TCS (Å^2)
0.01	12424.1	1.40	144.7	7.00	35.4	17	18.65	300	8.33
0.05	2222.8	1.60	129.7	7.50	31.8	18	19.66	400	7.09
0.10	1145.0	1.80	119.0	8.00	28.5	19	20.50	500	6.16
0.20	839.2	2.00	109.7	8.50	25.6	20	21.17	600	5.45
0.30	587.3	2.50	96.0	9.00	23.2	30	22.39	700	4.88
0.40	424.7	3.00	77.3	9.50	21.7	40	20.76	800	4.42
0.50	345.9	3.50	66.6	10.00	20.7	50	19.24	900	4.04
0.60	302.4	4.00	62.5	11.10	20.0	60	17.84	1000	3.71
0.70	270.1	4.50	56.4	12.01	20.2	70	15.92	2000	2.05
0.80	243.9	5.00	51.1	13.00	21.5	80	14.72	3000	1.40
0.90	222.8	5.50	47.3	14.00	20.5	90	13.93	4000	1.05
1.00	199.5	6.00	42.9	15.01	18.4	100	13.32	5000	0.84
1.20	166.4	6.50	38.6	16.00	17.8	200	10.11		

excitation at the energies $E_i \leqslant I$. However, if Δ is much less than the ionization threshold, then V_{abs} becomes unexpectedly high near the peak position and, to avoid such a situation for $E_i < E_p$, we have shown that Δ can be considered as the average excitation energy of the target and, in most cases, it is found to lie around $0.8I$ [50,56]. The amendment introduced by us is to give a reasonable minimum value of $0.8I$ to Δ. The parameter Δ is expressed as a function of E_i around I as

$$\Delta(E_i) = 0.8I + \beta(E_i - I), \tag{9}$$

where the value of the parameter β is obtained by requiring that $\Delta = I$ (eV) at $E_i = E_p$, i.e., the value of incident energy at which Q_{inel} reaches its peak. E_p can be found by calculating Q_{inel}, considering $\Delta = I$. Beyond E_p, Δ is kept constant and is equal to the ionization threshold I. The theoretical basis for assuming a variable Δ is discussed in more detail by Vinodkumar *et al.* [56].

The complex optical potential thus formulated is used to solve the Schrödinger equation numerically through partial wave analysis. This calculation will produce complex phase shifts for each partial wave, which describe the interaction of the incoming projectile with the target. The phase shifts (δ_i) thus obtained are employed to find the relevant cross sections, and the total elastic (Q_{el}) and total inelastic (Q_{inel}) cross sections using the scattering matrix $S_i(k) = \exp(2i\delta_i)$ [57]. The sum of these cross sections will then give the total scattering cross section (TCS), Q_T [58].

IV. RESULTS AND DISCUSSION

In the present work, we have carried out a comprehensive study of the collision of electrons with the MgO molecule in the gas phase. We report here the cross sections over a wide range of incident energies from 0.01 to 5000 eV. Our attempt in the present work is to compute the total cross section below the ionization threshold using close-coupling formalism employing the *R*-matrix method and beyond the ionization threshold using SCOP formalism. *R*-matrix calculations are computationally viable only up to 20 eV, while the SCOP formalism could be employed successfully from the ionization threshold of the target to 5000 eV. The results so obtained are consistent. Thus it is possible to provide the total cross section over a wide range of impact energies from meV to keV. Apart from total cross sections, we have also reported various target properties, resonances through an eigenphase sum study, electronic excitation cross sections, differential cross sections, momentum transfer cross sections, as well as scattering rate coefficients for low impact energies below 20 eV. We have presented our results in graphical form and numerical values of total cross sections are tabulated in Table III.

Table IV shows resonances for various doublet scattering states ($2A_1$, $2A_2$, $2B_1$, and $2B_2$) of the MgO system. It is important to study the eigenphase as we can deduce the

TABLE IV. Resonance positions and width (both in eV) for scattering states obtained using the *R*-matrix method along with the positions (eV) obtained using numerical double differential cross sections $\frac{d^2\sigma}{dE^2}$ (DDCS in $\frac{\mathring{A}^2}{eV}$) with respect to energy (e). Numbers in parentheses indicate the resonance number presented in Figs. 1 to 4.

Resonance state		Position (eV)		Width (eV)
		R matrix	DDCS	*R* matrix
$2A_1$	I		0.30 (1)	
	II		0.32 (2)	
	III	0.48	0.46 (3)	0.0027
	IV	0.48	0.49 (4)	0.0116
	V	1.67	1.66 (7)	0.0021
	VI		1.73 (8)	
	VII	2.71	2.72 (9)	0.0143
	VIII	4.44	4.79 (11)	0.1966
	IX		4.87 (12)	
	X	10.96	10.90 (14)	0.8734
	XI	11.26	11.28 (15)	0.0511
	XII	11.66	11.72 (17)	0.045
	XIII	11.75	11.72 (17)	0.0724
	XIV	12.18	12.16 (19)	0.2881
	XV	12.20	12.16 (19)	0.0003
$2B_1$	I	0.56		0.0145
$2B_2$	I	1.26	1.10 (5)	3.24×10^{-5}
	II		1.12 (6)	
	III	4.00	4.06 (10)	0.2095
	IV	8.80	8.79 (13)	0.0077
	V	11.54	11.48 (16)	0.1287
	VI	11.92	11.86 (18)	0.0217
	VII	11.96	11.86 (18)	0.0595
	VIII	13.09		0.9436
$2A_2$	I	0.49	0.49 (4)	0.0271
	II	2.25		0.0015
	III	8.72	8.79 (13)	0.2132
	IV	11.80	11.86 (18)	0.1146
	V	13.96	13.87 (20)	0.0537
	VI		14.09 (21)	
	VII	14.43	14.35 (22)	0.0104
	VIII		14.62 (23)	

position and width of resonances which lead to the important phenomenon of dissociative electron attachment (DEA) in the low-energy regime. Recently, DEA studies have gained prominence as they are indicative of the role of potential for controlling the chemistry driven by low-energy electrons. Due to the absence of theoretical data as well as experimental data for resonances, we have cross checked and confirmed our resonance data obtained through eigenphase analysis by performing double differentiation of TCS (DDCS) with respect to energy using numerical double differentiation by the five-point central difference formula [59]:

$$f''(E) = \frac{-2f(E-2h) + 16f(E-h) - 30f(E) + 16f(E+h) - f(E+2h)}{h^2}, \tag{10}$$

where f is a cross section as a function of energy and h equals the step size of the evenly distributed data on the energy grid.
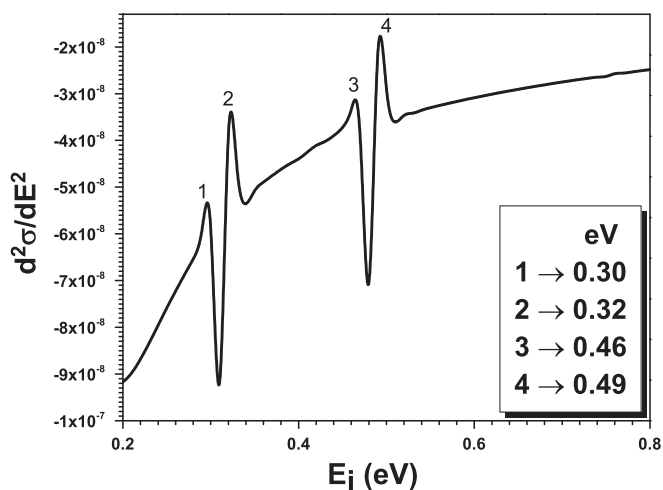
FIG. 1. Double differential cross sections (DDCS in $\mathring{A}^2$/eV) with respect to energy in the energy range 0.2 to 0.8 eV, indicating the resonance peaks. (Numbers over peaks indicate the resonance number.)

DDCS will give sharp peaks and valleys in the curve, at the resonance positions. We have reported the resonances obtained using the eigenphase sum and DDCS in Table IV. We have also plotted the DDCS curve against incident energy. For brevity of figures, we have divided the whole range of incident energy from 0.01 to 20 eV for DDCS in four plots. Figure 1 shows DDCS from 0.2 to 0.8 eV. The first two resonances (I and II) are reported at 0.30 and 0.32 eV from the DDCS curve, which are not seen in our eigenphase sum calculations. The third and fourth (III and IV) resonances are observed at 0.48 eV because $2A_1$ symmetry finds very good agreement with 0.46 and 0.49 eV obtained in our DDCS curve. Also, the first (I) resonance due to $2A_2$ symmetry is reported at 0.49 eV using the eigenphase sum and is in excellent agreement with data obtained from the DDCS curve. The first resonance using $2B_1$ symmetry is reported at 0.56 eV for which we do not find signature in our DDCS curve.

The second DDCS curve is from 1 to 3 eV (Fig. 2). The first (I) resonance due to the $2B_2$ state is reported at 1.26 eV using R-matrix calculations and is comparable to resonance at 1.10 eV using the DDCS curve. The fifth (V) resonance for the $2A_1$ state is at 1.67 eV and finds good agreement with resonance at 1.66 eV and is slightly lower compared to resonance at 1.73 eV observed in our DDCS curve. The second (II) resonance for $2A_2$ is obtained at 2.25 eV in our eigenphase study for which we have no signature in our DDCS curve. The seventh (VII) resonance at 2.71 eV due to $2A_1$ symmetry finds very good agreement with the resonance reported at 2.72 eV in the DDCS curve of Fig. 2. The third DDCS curve (Fig. 3) is for incident energies from 4 to 5 eV. The third (III) resonance for the $2B_2$ state is reported at 4.00 eV using the eigenphase sum and is in good agreement with the resonance observed at 4.06 eV in the DDCS curve. The eighth (VIII) resonance obtained at 4.44 eV for the $2A_1$ state using the eigenphase sum is slightly lower than the resonances observed at 4.79 and 4.87 eV in the DDCS curves of Fig. 3.

The fourth DDCS curve (Fig. 4) is for incident energies from 10.5 to 15 eV. The third (III) resonance for the $2A_2$
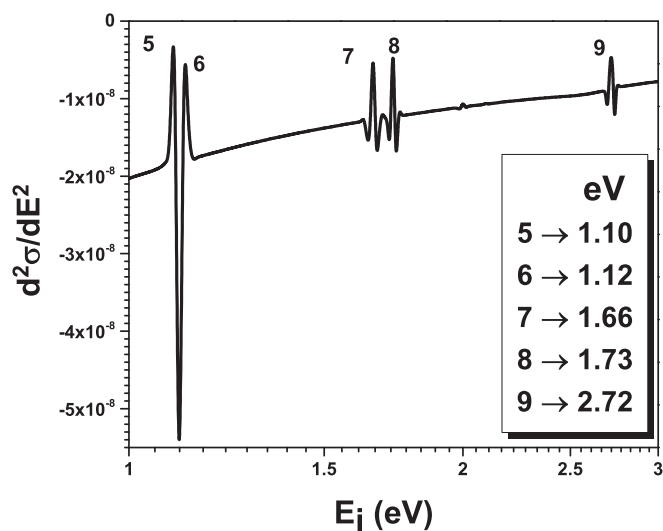

FIG. 2. Double differential cross sections (DDCS in $\mathring{A}^2$/eV) with respect to energy in the energy range 1 to 3 eV, indicating the resonance peaks. (Numbers over peaks indicate the resonance number.)

state and fourth (IV) resonance for the $2B_2$ state are reported at 8.72 and 8.80 eV, respectively, for which we get clear signature at 8.79 eV in our DDCS curve of Fig. 3. The tenth (X) resonance observed due to the $2A_1$ state at 10.96 eV in our eigenphase study is in good agreement with resonance at 10.90 eV observed in our DDCS curve. Above 11 eV, we find many resonances. The eleventh (XI) resonance due to $2A_1$ symmetry at 11.26 eV observed in the eigenphase study is in good agreement with the resonance at 11.28 eV in our DDCS curve, while the twelfth (XII) and thirteenth (XIII) resonances observed at 11.66 and 11.75 eV are comparable to the resonance observed at 11.72 eV in our DDCS curve. Similarly, the fifth resonance (V) is due to $2B_2$ symmetry reported at 11.54 eV for which we observe the peak at 11.48 eV
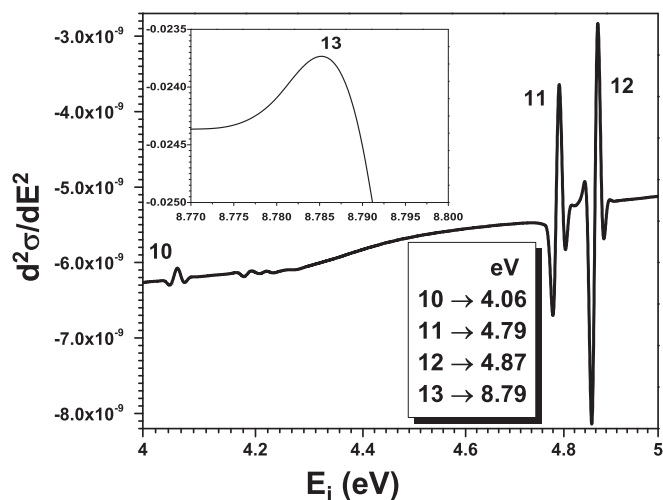

FIG. 3. Double differential cross sections (DDCS in $\mathring{A}^2$/eV) with respect to energy in the energy range 4 to 5 eV (inset: between 8.77 and 8.80 eV), indicating the resonance peaks. (Numbers over peaks indicate the resonance number.)
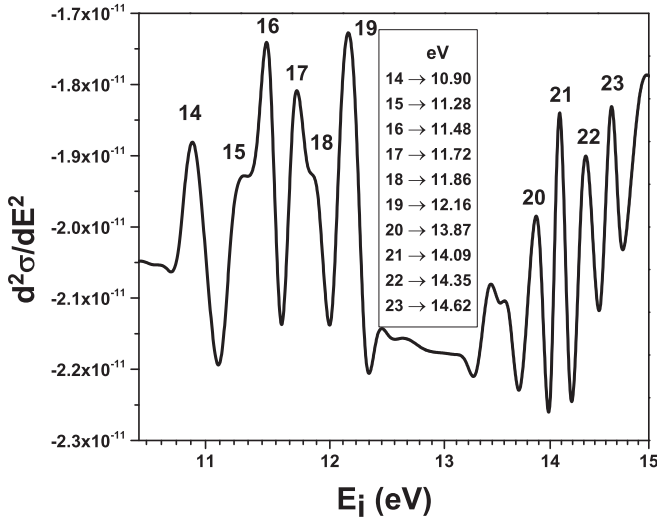
FIG. 4. Double differential cross sections (DDCS in $\mathring{A}^2$/eV) with respect to energy in the energy range 10.5 to 15 eV, indicating the resonance peaks. (Numbers over peaks indicate the resonance number.)

FIG. 5. MgO excitation cross section for a 34-state CC calculation from initial state $^1A_1$.

in our DDCS curve, while resonances reported at 11.92 eV (VI) and 11.96 eV (VII) in the eigenphase study are comparable to 11.86 eV observed in our DDCS curve. The fourth (IV) resonance reported at 11.80 eV for the $2A_2$ state is in very good agreement with the peak observed at 11.86 eV in our DDCS curve. The fourteenth and fifteenth (XIV and XV) resonances of the $2A_1$ state are reported at 12.18 and 12.20 eV for which we find clear signature at 12.16 eV in our DDCS curve of Fig. 4. The eighth (VIII) resonance of the $2B_2$ state is reported at 13.09 eV using the eigenphase sum for which we do not get any signature in the DDCS curve. The fifth (V) resonance of the $2A_2$ state is 13.96 eV using the eigenphase sum for which we get peaks at 13.87 and 14.09 eV in our DDCS curve in Fig. 4. Finally a seventh (VII) resonance for $2A_2$ symmetry is reported at 14.43 eV, which has a clear peak at 14.35 and 14.62 eV in our DDCS curve in Fig. 4.

These resonances reported in Table IV are reflected in the momentum transfer cross sections and also in our total cross-section curves. It is to be noted that as more states are included in the Close Coupling (CC) expansion and retained in the outer-region calculation, the eigenphase sum increases, reflecting the improved modeling of polarization interaction.

The two important contributions to the total inelastic cross sections are electronic excitation and ionization cross sections, apart from the contributions coming from nuclear motion, viz., rotational excitation and vibrational excitation. We have not considered contributions coming from nuclear motion as our basic assumption is a stationary nucleus. Figure 5 depicts the electronic excitation cross sections for ground state $1A_1$ to eight low-lying excited states ($3B_1$, $3B_2$, $1B_2$, $1B_1$, $3A_1$, $1A_1$, $3A_1$, and $3A_2$) for the 34-state CC calculation. Examining Table II, we find that $1A_1$ and $1A_2$, $3A_1$ and $3A_2$, and $3B_1$ and $3B_2$ are degenerate states. The excitation cross sections arising from the ground state to eight low-lying excited states are shown in Fig. 5. The maximum contribution to the excitation cross section comes from the two transitions from
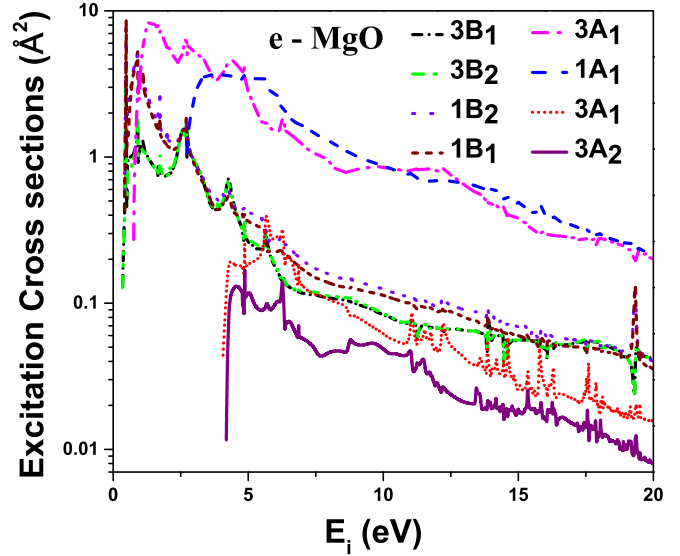
ground-state X $1A_1$ to 1 $3A_1$ and to 2 $1A_1$. These transitions show a sharp increase near their respective thresholds, indicating the dominance of these energy levels in the present calculation. It is important to note that for MgO, we get very high total electronic excitation cross sections of about 9 $\mathring{A}^2$. These cross sections reflect the probability of excitation to various energy levels of the target.

We have reported the differential cross sections for incident energies 1 to 10 eV, 15 eV, and 20 eV. We present the DCS results for 1, 3, 5, and 7 eV in Fig. 6. The scattering is dominated by elastic component $0 \rightarrow 0$ and dipole component $0 \rightarrow 1$. The elastic component shows a strong dip at $125°$ in the 1 eV curve, at $123°$ in the 3 eV curve, at $128°$ in the 5 eV curve, and at $50°$ and $127°$ in the 7 eV curve. These dips arise from
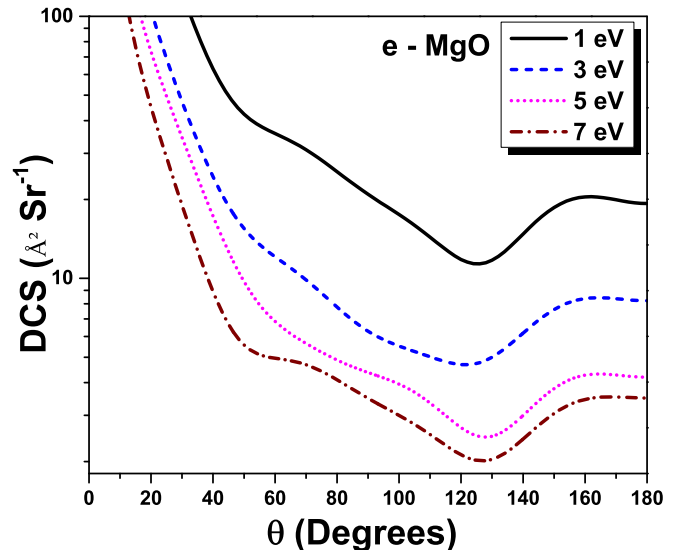

FIG. 6. Differential cross sections summed over all transitions for incident electron energies of 1, 3, 5, and 7 eV.
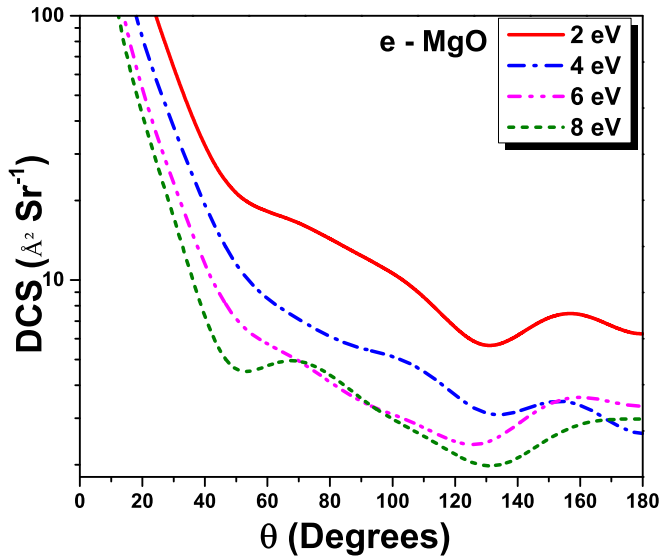
FIG. 7. Differential cross sections summed over all transitions for incident electron energies of 2, 4, 6, and 8 eV.

FIG. 8. Differential cross sections summed over all transitions for incident electron energies of 9, 10, 15, and 20 eV.

cancellations of attractive and repulsive potentials leading to very low scattering amplitudes and hence low values of the DCS at these angles. The contributions to differential cross sections from $J = 0$ to higher J diminish as expected.

In Fig. 7, we have shown DCS which are obtained by summing the rotational cross sections for all elastic components at selected energies of 2, 4, 6, and 8 eV. The divergence at the forward angle is confirmed as being due to dipole-allowed transitions $0 \rightarrow 1$ dominating the scattering. The differential cross sections decrease as the incident energy increases. The sharp enhancement in the forward direction is a result of the strong long-range dipole component of the interaction potential. For the 2 eV curve, we find a strong dip at 130°; for 4 eV, it is at 133°; for 6 eV, it is at 127°; and for 8 eV, it is at 51° and 131°. We notice that the position of these dips is almost the same for all of these curves. Finally, in Fig. 8, we have shown DCS for 9, 10, 15, and 20 eV; in all of these curves, we find two strong minima, as seen from Fig. 8. At 9 eV, these minima are at 52° and at 133°; for the 10 eV curve, at 51° and at 131°; for 15 eV, at 54° and 132°; and for 20 eV, at 54° and 127°. It is worth noting that the position of these minima in all of these curves lies almost at the same angles. We have not found other theoretical or experimental data to compare with these data sets for DCS.

In Fig. 9, the results for momentum transfer cross sections (MTCS) are presented in the range 0.01–20 eV. The MTCS are an indication of the amount of backward scattering. The MTCS are a useful observable for the swarm study of electrons through gases and it determines the electron distribution function through the solution of the Boltzmann equation and their drift velocity in the molecular gas. We observe that the MTCS decrease with increasing incident energies. In contrast to the divergent behavior of DCS at lower angles, the MTCS do not diverge due to the multiplicative factor $(1 - \cos\theta)$. The various peaks observed in the MTCS are the signatures of various resonances, which are shown in Table IV, and we find a good match between the two. The distinctive peak seen
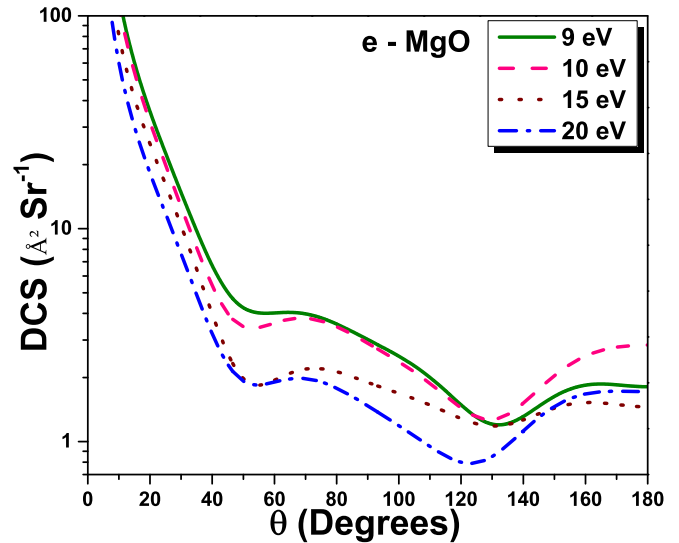
at 11.48 eV is the result of the large number of resonances reported in our eigenphase study as well as in DDCS curves from all symmetry states (Figs. 1–4).

Figure 10 represents the total cross sections for *e*-MgO scattering over a wide range of impact energies from 0.01 to 5000 eV. For brevity of figure, the total cross sections for 0.2 to 2.8 eV are shown in the inset as the magnitude of the cross section in this energy range is extremely high due to a strong dipole moment. Further, this figure clearly reflects various structures arising due to resonance processes. "1" in the inset figure corresponds to the peak at 0.48 eV, which may be attributed to two resonances: one at 0.48 eV due to $2A_1$ and the other at 0.49 eV due to $2A_2$ symmetry. The second feeble structure at position "2" and a very clear peak at 1.11 eV at position 3 are not reported in our resonance table. The
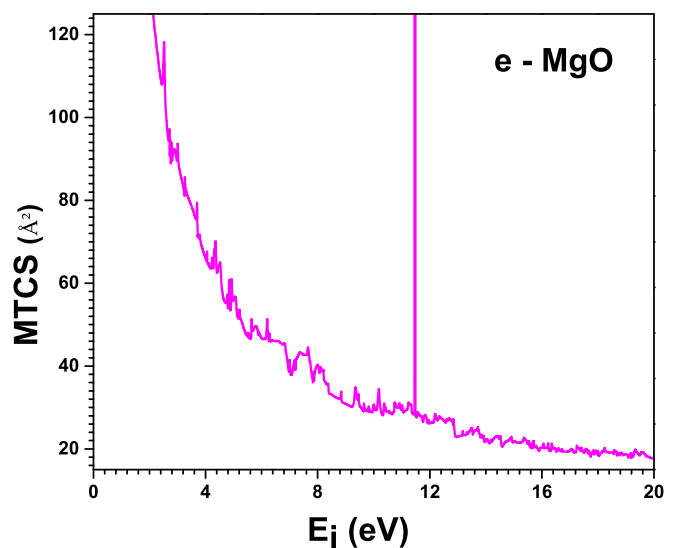

FIG. 9. Momentum transfer cross sections (MTCS) for electron MgO scattering ranging from the incident electron energy of 0.01 to 20 eV.
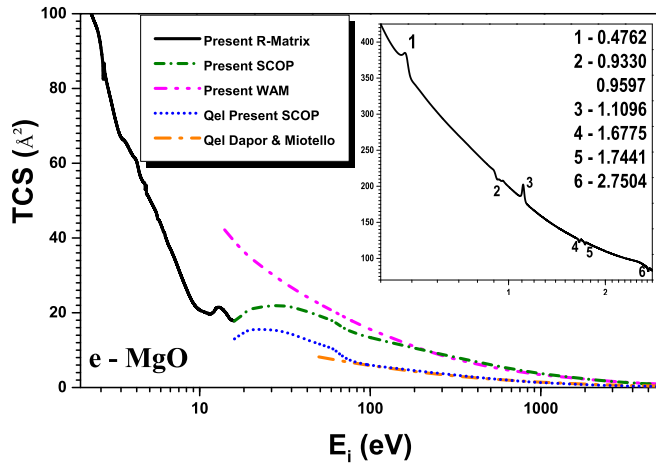
FIG. 10. Total cross sections (TCS) along with the elastic cross sections (Q_{el}) for e-MgO scattering.

small structure at position "4" at 1.68 eV is close to resonance at 1.67 eV due to $2A_1$ symmetry. The structure reflected at position "5" at 1.74 eV finds no predictions by our R-matrix calculation.

It is quite clear from the curve that there is a smooth matching of results obtained by the R-matrix formalism and SCOP formalism at about 16 eV. We have also performed high-energy calculations using the weighted additivity method (WAM) [60,61], which also finds excellent agreement with the SCOP results beyond 160 eV. The total elastic cross sections (Q_{el}) are also presented in Fig. 10. Our Q_{el} data find very good agreement both quantitatively and qualitatively with the data of Dapor and Miotello [18] above 75 eV, below which they are slightly higher.

Finally, electron impact scattering rate coefficients are plotted as a function of the kinetic temperature (Fig. 11), which is defined according to the Maxwell-Boltzmann distribution. From this graph, it is noted that the scattering rate increases rapidly up to approximately 290 K before gradually dying down as the temperature is further increased. The maximum
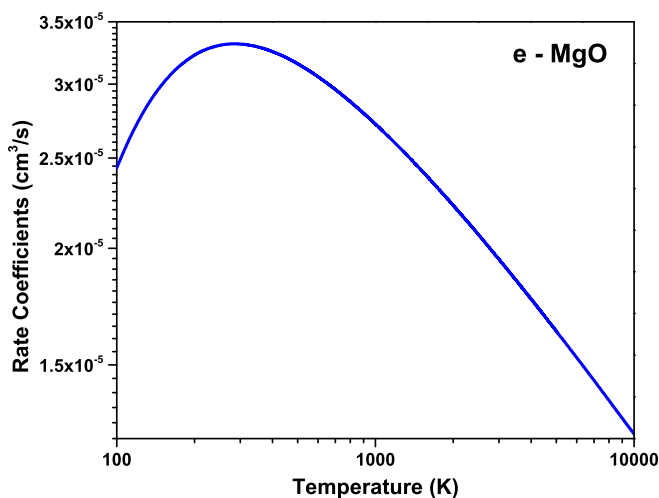

FIG. 11. Total rate coefficients for e-MgO elastic scattering.

rate coefficient value is 3.31×10^{-5} cm^3/s at 290 K. Once again, we did not find any data with which to compare our presented values.

V. CONCLUSION

We report a detailed *ab initio* study of e-MgO scattering. This includes various target properties, resonances through eigenphase study as well as DDCS, vertical electronic excitations and differential, momentum transfer, and total cross sections along with scattering rate coefficients in the article. We get very good agreement for all target properties listed in Table I with data available in the literature. There is a large number of electronic excited states in MgO and the present data is close to many earlier predictions (see Table II). The important component of low-energy studies is resonances, which are reported here for all four doublet states ($2A_1$, $2A_2$, $2B_1$, $2B_2$). In the absence of any comparisons, either experimental or theoretical, we have deduced resonances using the eigenphase sum and reconfirmed through double differentiation of the TCS (DDCS). All DCS curves for 1 to 10 eV, 15 eV, and 20 eV and also MTCS are our maiden efforts. At low energy, the elastic cross sections diverge due to the effect of the strong dipole moment. There are many resonances observed around 11 eV, as listed in Table IV. They are reflected in MTCS as well as TCS as a prominent structure around 11.48 eV. The present total elastic cross sections find very good agreement both quantitatively and qualitatively with a single set of theoretical results by Dapor and Miotello [18].

We have performed 34-state close-coupling calculations employing the UK molecular R-matrix code below the ionization threshold of the target, while SCOP formalism is used beyond it. We have demonstrated through Fig. 10 that the results using these two formalisms are consistent and show a smooth crossover at the overlap energy ($\sim$16 eV). This feature confirms the validity of our theories and hence enables us to predict the total cross sections from thermal energy of the target (0.01 eV) to high energy (5000 eV) [21,22,43,44].

We are confident that this methodology may be employed further to calculate total cross sections over a wide range of impact energies in other molecular systems where experiments are difficult or not possible to perform. Total cross-section data finds importance in a variety of applications, from aeronomy to plasma modeling. Accordingly, such a methodology may be built into the design of an online database to provide the "data user" with the opportunity to request their own set of cross sections for use in their own research. Such a prospect will be explored by the emerging Virtual Atomic and Molecular Data Centre (VAMDC) [62].

[1] J. Schamps and H. LefebvreBrion, J. Chem. Phys. **56**, 573 (1972).

[2] C. W. Bauschlicher, Jr., D. M. Silver, and D. R. Yarkony, J. Chem. Phys. **73**, 2867 (1980).

[3] C. W. Bauschlicher, B. H. Lengsfield III, D. M. Silver, and D. R. Yarkony, J. Chem. Phys. **74**, 2379 (1981).

[4] B. Huron and P. Rancurel, Chem. Phys. Lett. **13**, 515 (1972).

[5] H. Thummel, R. Iuotz, and S. D. Peyerimhoff, Chem. Phys. **129**, 417 (1989).

[6] B. Rosen, *Spectroscopic Data Relative to Diatomic Molecules* (Pergamon Press, Oxford, 1970).

[7] K. P. Huber and G. Herzberg, in *Molecular Spectra and Molecular Structure* (Van Nostrand Reinhold, New York, 1979), p. 550.

[8] J. H. Kim, X. Li, L. S. Wang, H. L. de Clercq, C. A. Fancher, O. C. Thomas, and K. H. Bowen, J. Phys. Chem. A **105**, 5709 (2001).

[9] B. Bourguignon, J. McCombie, and J. Rostas, Chem. Phys. Lett. **113**, 323 (1985).

[10] L. Brewer and S. Trajmar, J. Chem. Phys. **36**, 1585 (1962).

[11] T. Ikeda, N. B. Wong, D. O. Harris, and R. W. Field, J. Mol. Spectrosc. **68**, 452 (1977).

[12] A. Lagerqvist and U. Uhler, Nature **164**, 665 (1949).

[13] J. K. A. Clarke, M. J. Bradley, L. A. J. Garvie, A. J. Craven, and T. Baird, J. Catal. **143**, 122 (1993).

[14] J. B. Johnson and K. G. McKay, Phys. Rev. **91**, 582 (1953).

[15] W. W. Duley Astrophys. Space Sci. **47**, 185 (1977).

[16] S. MacLean and W. W. Duley, Astrophys. J. **252**, L25 (1982).

[17] J. B. Pedley and E. M. Marshall, Phys. Chem. Ref. Data **12**, 967 (1983).

[18] M. Dapor and A. Miotello, Eur. Phys. J. AP **5**, 143 (1999).

[19] J. Tennyson, D. B. Brown, J. Munro, I. Rozum, H. N. Varambhia, and N. Vinci, J. Phys.: Conf. Ser. **86**, 012001 (2007).

[20] H. N. Varambhia, J. J. Munro, and J. Tennyson, Int. J. Mass Spectrosc. **271**, 1 (2008).

[21] M. Vinodkumar, H. Desai, and P. C. Vinodkumar, RSC Adv. **5**, 24564 (2015).

[22] M. Vinodkumar, C. Limbachiya, H. Desai, and P. C. Vinodkumar, J. Appl. Phys. **116**, 124702 (2014).

[23] D. R. Lide, *CRC Handbook of Physics and Chemistry*, 74th ed. (Chemical Rubber Company, Boca Raton, FL, 1993).

[24] J. Tennyson, J. Phys. B: At., Mol. Opt. Phys. **29**, 6185 (1996).

[25] H. N. Varambhia, Ph.D. dissertation (University College, London, 2010).

[26] P. Piyykko, H. F. Geerd, and F. Muller, Chem. Phys. Lett. **141**, 535 (1987).

[27] A. D. McLean and M. Yoshimine, IBM J. Res. Dev. Suppl. **13**, 206 (1967).

[28] P. Mürtz, H. Thümmel, C. Pfelzer, and W. Urban, Mol. Phys. **86**, 513 (1995).

[29] http://cccbdb.nist.gov (unpublished).

[30] B. I. Schneider and T. N. Rescigno, Phys. Rev. A **37**, 3749 (1988).

[31] T. N. Resigno, C. W. McCurdy, A. E. Orel, and B. H. Lengsfield III, in *Computational Methods for Electron Molecule Collisions*, edited by W. M. Huo and F. Gianturco (Plenum, New York, 1995), pp. 1–44.

[32] K. Takatsuka and V. McKoy, Phys. Rev. A **24**, 2473 (1981).

[33] K. Takatsuka and V. McKoy, Phys. Rev. A **30**, 1734 (1984).

[34] C. Winstead, Q. Y. Sun, P. G. Hipes, M. A. P. Lima, and V. McKoy, Aust. J. Phys. **45**, 325 (1992).

[35] D. Bouchiha, J. D. Gorfinkiel, L. G. Caron and L. Sanche, J. Phys. B: At. Mol. Opt. Phys. **40**, 1259 (2007).

[36] J. Tennyson, Phys. Rep. **491**, 29 (2010).

[37] C. J. Noble and R. K. Nesbet, Comput. Phys. Commun. **33**, 399 (1984).

[38] A. M. Arthurs and A. Dalgarno, Proc. Phys. Soc., London, Sect. A **256**, 540 (1960).

[39] A. Faure, J. D. Gorfinkiel, L. A. Morgan, and J. Tennyson, Comput. Phys. Commun. **144**, 224 (2002).

[40] S. I. Chu and A. Dalgarno, Phys. Rev. A **10**, 788 (1974).

[41] M. Gailitis, J. Phys. B: At. Mol. Opt. Phys. **9**, 843 (1976).

[42] J. Tennyson and C. J. Nobel, Comput. Phys. Commun. **33**, 421 (1984).

[43] M. Vinodkumar, C. Limbachiya, H. Desai, and P. C. Vinodkumar, RSC Adv. **5**, 69466 (2015).

[44] M. Vinodkumar, C. Limbachiya, H. Desai, and P. C. Vinodkumar, Phys. Rev. A **89**, 062715 (2014).

[45] F. A. Gianturco and A. Jain, Phys. Rep. **143**, 347 (1986).

[46] N. Sanna and F. A. Gianturco, Comput. Phys. Commun. **114**, 142 (1998).

[47] C. Limbachiya, M. Vinodkumar, and N. Mason, Phys. Rev. A **83**, 042708 (2011).

[48] M. Vinodkumar, H. Bhutadia, B. Antony, and N. Mason, Phys. Rev. A **84**, 052701 (2011).

[49] M. Vinodkumar, C. Limbachiya, K. Korot, and K. N. Joshipura, Eur. Phys. J. D **48**, 333 (2008).

[50] M. Vinodkumar, K. Korot, and P. C. Vinodkumar, Int. J. Mass Spectrosc. **305**, 26 (2011).

[51] C. F. Bunge and J. A. Barrientos, At. Data Nucl. Data Tables **53**, 113 (1993).

[52] S. Hara, J. Phys. Soc. Jpn. **22**, 710 (1967).

[53] X. Zhang, J. Sun, and Y. Liu, J. Phys. B **25**, 1893 (1992).

[54] G. Staszewska, D. W. Schwenke, and D. G. Truhlar, J. Chem. Phys. **81**, 335 (1984).

[55] G. Staszewska, D. W. Schwenke, and D. G. Truhlar, Phys. Rev. A **29**, 3078 (1984).

[56] M. Vinodkumar, K. Korot, and P. C. Vinodkumar, Eur. Phys. J. D **59**, 379 (2010).

[57] C. J. Joachain, *Quantum Collision Theory* (North-Holland, Amsterdam, 1983).

[58] P. Lamão-Vieira, F. Blanco, J. C. Oller, A. Muñoz, J. M. Pérez, M. Vinodkumar, G. García, and N. J. Mason, Phys. Rev. A **71**, 032720 (2005).

[59] E. Balagurusamy, *Numerical Methods* (Tata/McGraw-Hill, New Delhi, 1999), p. 361.

[60] H. Desai, M. Vinodkumar, and P. C. Vinodkumar, in *Electron Collision Processes in Atomic and Molecular Physics*, edited by M. Vinodkumar (Narosha Publishing House, New Delhi, 2014), p. 61.

[61] H. Desai, M. Vinodkumar, and P. C. Vinodkumar, *Theoretical Estimations of Electron Impact Collision Cross Sections* (Lambert, Germany, 2014).

[62] M. L. Dubernet *et al.*, J. Quantum Spectrosc. Radiat. Transf. **111**, 2151 (2010).